Japan Architectural Review
Open Access

Architectural Institute of Japan

Original Paper

Implicit finite element analysis of ductile fracture of a steel frame under cyclic deformation

Makoto Ohsaki[1] Jun Fujiwara,[2] Tomoshi Miyamura[3] and Hisashi Namba[4]

[1]Department of Architecture and Architectural Engineering, Graduate School of Engineering, Kyoto University, Kyoto, Japan; [2]National Research Institute for Earth Science and Disaster Resilience, Miki, Japan; [3]Department of Computer Science, College of Engineering, Nihon University, Koriyama, Japan
[4]Department of Architecture, Kobe University, Kobe, Japan

Correspondence
Makoto Ohsaki, Department of Architecture and Architectural Engineering, Graduate School of Engineering, Kyoto University, Kyoto, Japan
Email: ohsaki@archi.kyoto-u.ac.jp

Funding information
Japan Society for the Promotion of Science, Grant/Award Number: KAKENHI No. JP19H02286

Received May 7, 2021; Accepted March 2, 2022

doi: 10.1002/2475-8876.12264

Abstract

A ductile fracture model is implemented to an elastoplastic constitutive model of steel material for large-scale finite element analysis of steel frames. The stress modified critical strain model is extended to simulate the structural response after initiation of ductile fracture. The yield stress, Young's modulus, as well as the stress are reduced using the fracture variable. Positive definiteness of the material tangent stiffness matrix is always maintained, and the unbalanced loads are carried over to the succeeding step to analyze the responses in the range of degrading strength using an implicit finite element analysis. It is shown using a notched rod model and a double notched plate that the proposed model can simulate steep stiffness degradation due to strain localization after ductile fracture. Applicability to a large-scale finite element analysis is investigated using a component frame of moment frame subjected to cyclic forced deformation.

Keywords
cyclic loading, ductile fracture, finite element analysis, steel frame, stress triaxiality

1. Introduction

Precise simulation of collapse behavior of a steel frame under cyclic deformation is necessary to be carried out for investigation of hazard and risk under unexpectedly large seismic motions. Especially, the fracture behavior at the beam-to-column joints is important for accurate evaluation of seismic performance of a steel frame,[1] because frame collapses after ductile stiffness degradation at the joints. Although various studies can be found for collapse analysis of building frames considering fracture at joints and members, most of them utilize frame and hinge models,[2,3] and accuracy of the structural behavior after strength degradation strongly depends on the quality of the hinge model. The adaptively shifted integration (ASI) model developed by Isobe and Toi[4] may be effectively used for accurate simulation of collapse behavior including the progressive collapse. However, it is difficult to simulate the complex ductile fracture at the beam-to-column joints using a frame model with plastic hinges. The stress distribution in the section is not considered using the hinge model. Therefore, the complex behavior due to, for example, effect of local buckling of flange on the initiation of ductile fracture cannot be simulated accurately using a hinge model.

Recently, finite element (FE) analysis has been applied to simulate ductile fracture of steel frames.[5,6] Mizushima et al.[7] predicted initiation of fracture at the beam-to-column joint of a three-story steel frame subjected to seismic excitation using an explicit time integration method. Wang et al.[8] carried out FE-analysis for predicting ductile fracture at the joint. In these studies, however, behavior after fracture cannot be simulated. Sawamoto and Ohsaki[9] proposed a model for incorporating re-contact after fracture under cyclic deformation by placing a nonlinear spring element in the region where fracture is expected to occur. Removing elements is possible if an explicit time integration method is used. However, it is generally not possible to predict the locations of fracture a priori, and simulation of strength reduction after fracture is very difficult when an implicit FE-analysis is used. The deformation will concentrate at the fractured part with degrading stiffness, and the reaction force decreases in the process of forced displacement analysis. Consequently, Newton–Raphson iteration stops because convergence cannot be achieved. Therefore, analysis cannot continue even the fractured part is very small.

Various models have been proposed for ductile fracture and ultra-low cycle fatigue of steel material. Simple models such as Manson–Coffin law are based on the number of cycles of plastic deformation, and a modified law has been proposed by Huang and Mahin.[10] Since the damage leading to fracture is accumulated in a tensile stress state, the stress triaxiality should be taken into consideration for simulating ductile

fracture.[11,12] For example, stress modified critical strain (SMCS) criterion[13-16] defines the critical value of accumulated plastic strain based on the stress triaxiality. Ohsaki and Nakajima[17] optimized the locations of stiffener plates for improving the performance of an eccentrically braced frame under cyclic deformation using the SMSC criterion. Various criteria have been proposed for ductile fracture of steel material under cyclic loading. Kanvinde et al.[18] simulated fracture initiation of link member of an eccentrically braced frame using a failure index based on stress triaxiality. However, most of the criteria for ductile fracture are used for predicting initiation of the fracture, and analysis after fracture is very difficult.

An FE-analysis program called E-Simulator is under development at the Hyogo Earthquake Engineering Research Center of the National Research Institute for Earth Science and Disaster Resilience (NIED), Japan, which has world's largest shaking table called E-Defense. E-Simulator is based on the software called ADVENTURECluster[19] that is developed for large-scale and high-precision FE-analysis. Ohsaki et al.[20] proposed a simple semi-implicit plastic constitutive model for large-scale FE-analysis of steel structures. They implemented the model in E-Simulator, and applied it to simulation of E-Defense experiment of total collapse behavior of a four-story frame.[21,22] It has also been shown that the collapse behavior of a composite beam can be precisely simulated using the semi-implicit model.[23,24] However, ductile fracture of steel material has not been incorporated. Note that stiffness degradation due to necking can be simulated using an elastoplastic constitutive low without considering ductile fracture.[25,26]

Ductile damage and degradation of stiffness and strength due to initiation and growth of voids can be simulated using various models of damage plasticity, or damaged plasticity, in the field of continuum damage mechanics (CDM).[27,28] Damage plasticity model has also been developed for concrete material.[29] Development of theories and methods for ductile fracture analysis in the field of CDM is summarized in Ref. [30] The process of stiffness degradation due to ductile damage and fracture can be simulated using the Gurson model.[31,32] The consistent tangent matrix for FE-analysis based on the Gurson model has been derived.[33] However, because the Gurson model simulates the growth of void, it inherently involves stiffness degradation; therefore, it is difficult to achieve convergence using an implicit time integration method. By contrast, substantial computational cost is required if explicit time integration method is used for nonlinear response history analysis of a frame subjected to a long-term seismic motion. Therefore, a method of ductile fracture needs to be developed for application to large-scale implicit FE-analysis. However, the response after fracture is difficult to simulate by simple application of implicit time integration, because the Newton–Raphson iteration for achieving equilibrium cannot converge in the range of degrading stiffness.

In this paper, a method is proposed for precisely predicting the stiffness deterioration behavior of steel frames due to ductile fracture of material. The authors incorporate a ductile fracture model based on the SMCS criterion considering the stress triaxiality into the semi-implicit elastoplastic constitutive model proposed by the authors previously.[20] The fracture model is implemented to ADVENTURECluster as a user function. Using the proposed procedure, positive definiteness of the material tangent stiffness matrix is always maintained, and unstable response after fracture is simulated by carrying over the unbalanced force to the next step, while maintaining stability during Newton–Raphson iteration. Uniaxial tension analysis is carried out for a notched rod and a double notched plate to verify the accuracy and ability of simulating degrading stiffness and strength after fracture. Applicability of the model to a large-scale FE-analysis is investigated by static cyclic analysis of a beam-column model.

2. Ductile Fracture Model for FE-analysis

The elastoplastic cyclic constitutive model[20] developed by the authors is extended to incorporate the ductile fracture. The model is based on a piecewise-linear isotropic-kinematic hardening. In the similar manner as the standard approach of CDM, a *fracture variable* is defined as a function of the equivalent plastic strain. Here, we use the SMCS criterion considering the stress triaxiality to detect the initiation of ductile fracture, and extend it to the analysis after fracture.

Let σ_m and σ_e denote the mean and equivalent stresses, respectively. The variable T representing the stress tri-axiality is defined as follows:

$$T = \frac{\sigma_m}{\sigma_e} \tag{1}$$

Note that $T = 1/3$ for the uniaxial tension state and $T = 2/3$ for the uniform biaxial tension state. Although T diverges to infinity for the hydrostatic state, such situation is not expected for steel members composed of thin plates, which may be approximated by the plane stress state, that is, the out-of-plane stress components are zero.

It should be noted here that ductile fracture of steel material is related to the void growth exhibited in a tensile state. Therefore, fractured state is determined using the representative plastic strain $\hat{\varepsilon}^p$ obtained by integrating the equivalent plastic strain rate $\dot{\varepsilon}^p$ in the tensile state with $\sigma_m > 0$ ($T > 0$). The critical value of $\hat{\varepsilon}^p$ for ductile fracture, which is denoted by ε^c and simply called fracture strain, is defined using T as in Ref. [13]

$$\varepsilon^c = \beta \exp(-1.5T) \tag{2}$$

where β is a material parameter. Hence, the fractured state is determined by

$$\hat{\varepsilon}^p \geq \varepsilon^c = \beta \exp(-1.5T) \tag{3}$$

Difference between the integrated absolute values of $\dot{\varepsilon}^p$ in tensile and compressive states, respectively, is used in Ref. [15] for the condition in Equation (3). Lemaitre[28] defined the damage variable using the elastic strain energy and two material parameters, and integrated the variable when the largest principal stress is positive. In Refs. [9, 10], $\dot{\varepsilon}^p$ is integrated when $T > -1/3$. However, we use a simple condition $\sigma_m > 0$ that expresses the tensile state.

For simpler presentation of fracture condition, the deformation parameter α is defined as

$$\alpha = \hat{\varepsilon}^p \exp(1.5T) \tag{4}$$

and the condition for ductile fracture, which is represented by Equation (3), is written as

$$\alpha \geq \beta \tag{5}$$

In the uniaxial state with $T = 1/3$, α is equal to $e^{0.5}\hat{\varepsilon}^p = 1.649\hat{\varepsilon}^p$.

The parameter β depends on the material. In Ref. [18], $\beta = 2.6$ and 1.0 are calibrated for the base metal and the heat

affected zone, respectively, of A572 Grade 50 steel. The coefficient 1.5 in Equations (2)–(4) is theoretically derived in Ref. [11]; however, different values between 1.1 and 2.3 may be recommended depending on the steel material properties.[12] Furthermore, the fracture strain depends on the characteristic length of the ductile crack, which is between 0.09 mm and 0.38 mm.[16] The size of FE-mesh should also be considered for the condition of ductile fracture when stress concentration exists.

As explained in the introduction, the element can be removed after fracture when the explicit time integration method is used.[9] However, removal of element during FE-analysis may lead to more drastic reduction of load bearing capacity of the structure than the experimental result.[9] Therefore, we reduce the stiffness and strength at each integration point of the fractured element using the fracture variable D, and express D as a piecewise linear function of the deformation parameter α, where $D = 0$ before fracture, and D takes a value between 0 and 1. Note that D does not represent the effect of void growth on stiffness degradation of the material before fracture. It is used for modeling reduction of the stiffness after initiation of ductile fracture. Degradation of hardening coefficient before fracture is modeled within the framework of elastoplastic material so that the hardening coefficient does not become negative. For example, for a case with four segments, the relation between α and D is written as

$$D = \begin{cases} 0 & (\alpha \le \alpha_1 = \beta) \\ \dfrac{D_1}{\alpha_2 - \alpha_1}(\alpha - \alpha_1), & (\alpha_1 \le \alpha \le \alpha_2) \\ \alpha_2 + \dfrac{D_2 - D_1}{\alpha_3 - \alpha_2}(\alpha - \alpha_2) & (\alpha_2 \le \alpha \le \alpha_3) \\ D_2 & (\alpha_3 \le \alpha) \end{cases} \tag{6}$$

which is illustrated in Figure 1. Note that fracture occurs at $\alpha = \alpha_1 = \beta$, which is equal to β in Equation (5).

To prevent steep reduction of the nodal loads after fracture, we gradually increase D in Equation (2) at each integration point, and reduce Young's modulus, yield stress, hardening coefficient, and stress at the integration point. This way, degradation of the stiffness and strength develops gradually. The parameter values for modeling cyclic elastoplastic property are the same as Ref. [20] if not explicitly specified. Note that the effect of yield plateau is neglected, because it is irrelevant to a monotonic loading in Sections 3 and 4, and fracture in a large strain range is investigated in Section 5. The linear hexahedral solid element with selective reduced integration is used; that is, the integration corresponding to the volumetric strain is carried out only at the center of the element, while integration is carried out at the eight integration points for the deviatoric strain components. The appropriate value of each fracture parameter depends on the material and mesh size. However, no experimental investigation has been done for the fracture properties of materials used in the following numerical examples. Therefore, we assign the α_1 value for initiation of fracture heuristically. The value of D_3 should be close to 1; however, 0.9 or 0.95 is assigned because the convergence may not be achieved if $D_3 = 0.99$. The values of α_2 and D_2 are assigned so that fracture after its initiation proceeds moderately.

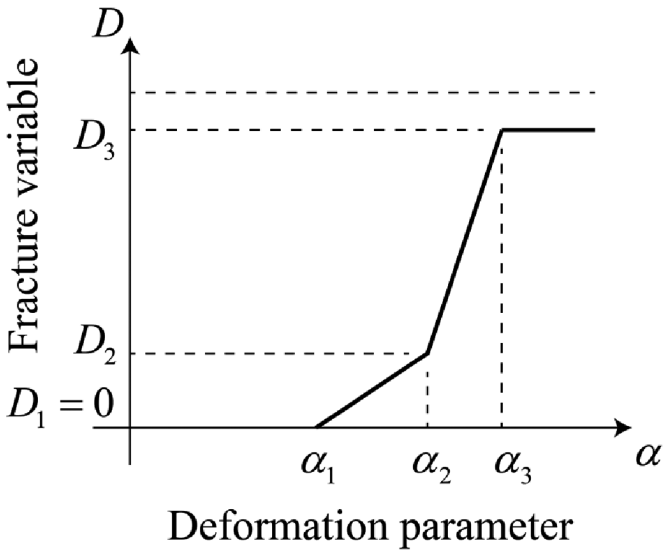

FIGURE 1. Piecewise linear relation between deformation parameter α and fracture variable D for a case with four segments

It should be noted here that the tangent stiffness matrix used for Newton–Raphson iteration for achieving equilibrium is always positive definite in the proposed method, because D is kept constant during the increment. Thus, convergence is ensured even at the unstable state after fracture. Young's modulus E, yield stress (current radius of the yield surface in the deviatoric stress space) σ_Y, back stress tensor $\boldsymbol{\sigma}_0$, hardening coefficient H, and stress tensor $\boldsymbol{\sigma}$ are scaled by the ratio $1-D$ using the updated value of D after convergence, and the corresponding unbalanced loads are carried over to the next step to be added to the load increment. Therefore, the equilibrium state after convergence of Newton–Raphson iteration is a tentative state; however, the unbalanced force is negligibly small and can be reduced in the next step if a small increment is adopted. The outline of the algorithm for an incremental process of the load vector $\mathbf{P}$ is as follows:

Algorithm

1 Newton–Raphson iteration for increment k

1.1 Compute displacement increment.
1.2 For all integration points of all elements:
Compute H, ε^p, $\boldsymbol{\sigma}$, σ_e, σ_m, T, and increment $\Delta\varepsilon^p$ of ε^p from the previous step.
1.3 Compute unbalanced forces and go to 1.1 if not converged.

2 Reduction of stiffness and strength after increment k:

For all integration points of all elements:
Update $\hat{\varepsilon}^p$ to $\hat{\varepsilon}^p + \Delta\varepsilon^p$ if $\sigma_m > 0$, and compute fracture variable D_k.
If $D_k > D_{k-1}$:
Compute $R = (1-D_k)/(1-D_{k-1})$.
$\boldsymbol{\sigma} \leftarrow R\boldsymbol{\sigma}$, $\sigma_Y \leftarrow R\sigma_Y$, $\boldsymbol{\sigma}_0 \leftarrow R\boldsymbol{\sigma}_0$, $E \leftarrow RE$, $H \leftarrow RH$
Compute internal force vector and the unbalanced force vector $\mathbf{R}$.
Update the load vector and add the unbalanced force vector as $\mathbf{P} \leftarrow \mathbf{P} + \Delta\mathbf{P} + \mathbf{R}$, $k \leftarrow k + 1$ and go back to 1.

3. Notched Rod Model

FE-analysis is carried out for the uniaxial test of a notched rod in Ref. [34]. The hardening property is identified using the

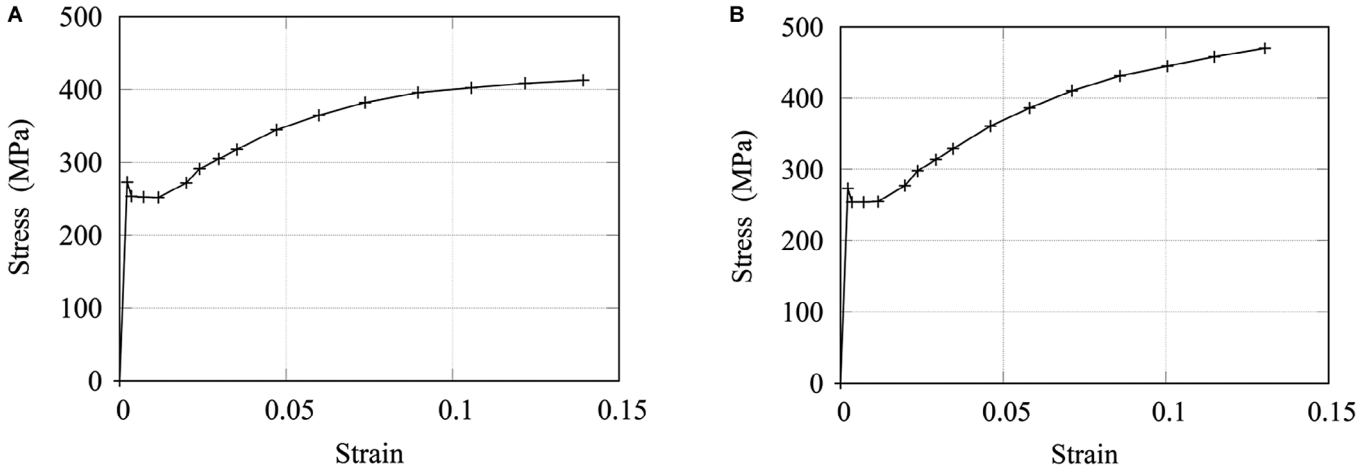

FIGURE 2. Relation between stress and strain of rod without notch; (A) nominal values,[34] (B) true values

experimental result of the rod without notch in Ref. [34]. The relation between the nominal stress σ_0 and engineering strain ε_0 is shown in Figure 2(a), which is transformed into the relation between the true stress $\sigma_t = (1 + \varepsilon_0)\sigma_0$ and the logarithmic strain $\varepsilon_t = \log(1 + \varepsilon_0)$ as shown in Figure 2B. Note that ductile fracture was not observed in this test.

The stress–strain relation is modeled as a piecewise linear relation, and the hardening coefficients are identified using the curve (experimental result) in Figure 2B. A lower bound is assigned for the hardening coefficient, and its value beyond the final strain 0.1304 in the experiment is assumed to be 384 MPa, which is 1/50 of Young's modulus $E = 192$ GPa. The relation between the nominal stress σ_0 and engineering strain ε_0 obtained by uniaxial tension analysis of a single element is shown in Figure 3, which is close to the relation in Figure 2A.

The notched rod shown in Figure 4 is stretched in the axial direction by the forced displacements at both ends.[34] The material parameters are the same as the single element model. The value of α_1 $(= \beta)$ at the initiation of fracture is 2.60 based on the result in Ref. [12]. The parameters in Figure 1 are $(\alpha_1, D_1) = (2.60, 0.0)$, $(\alpha_2, D_2) = (2.65, 0.2)$, $(\alpha_3, D_3) = (2.70, 0.9)$ to prevent sudden decrease of stiffness and strength of the rod and to continue analysis after initiation of ductile fracture without divergence of the solution.

By utilizing symmetry of the rod and loading condition, and accordingly, symmetry of deformation, one of the 1/8 parts is discretized into hexahedral elements, as shown in Figure 5, in the similar manner as Ref. [34]. Symmetric boundary conditions are assigned along the internal boundaries, and forced axial displacements are given at the left end as illustrated in Figure 5. The nominal size of the mesh for automatic mesh generation is 0.1625 mm, and the numbers of nodes and elements are 78 710 and 71 680, respectively. Figure 5C shows the mesh on the surface, and the corner points and (x, y) coordinates are indicated in the figure, where z-coordinate is perpendicular to the plane. The (x, y) coordinates (mm) of points A, B, C, D, E, and F are (0, 0), (0, 5), (0, 30), (12.5, 25), (12.5, 3.5), and (5.5, 0), respectively. The displacement in x-direction and the rotations around y- and z-axes are fixed on the boundary AC, and the displacement in y-direction and the rotations around x- and z-directions are fixed on the boundary AF. A uniform y-directional displacement is given on the free boundary CD. The axial displacements at points A and B located on the surface are extracted to obtain the relative displacement U. The displacement increment at the left end is fixed at 0.001 mm.

The load–displacement relation obtained by the experiment in Ref. [34] is plotted with dotted line in Figure 6, which shows that the load has the peak around the displacement $U = 0.7$ mm and decreases until fracture occurs at around $U = 2$ mm. The

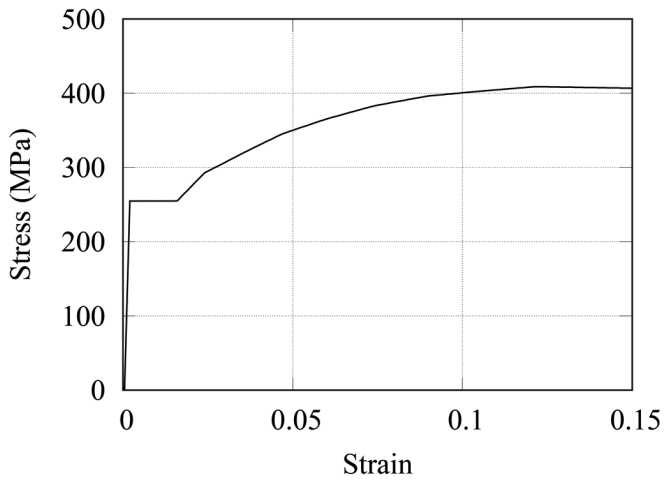

FIGURE 3. Tensile stress–strain relation of a single element

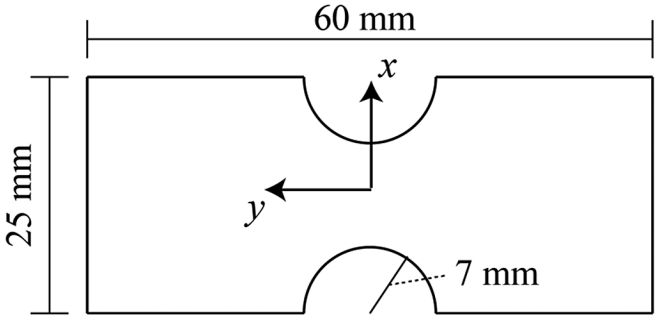

FIGURE 4. A notched rod model with thickness 12.7 mm

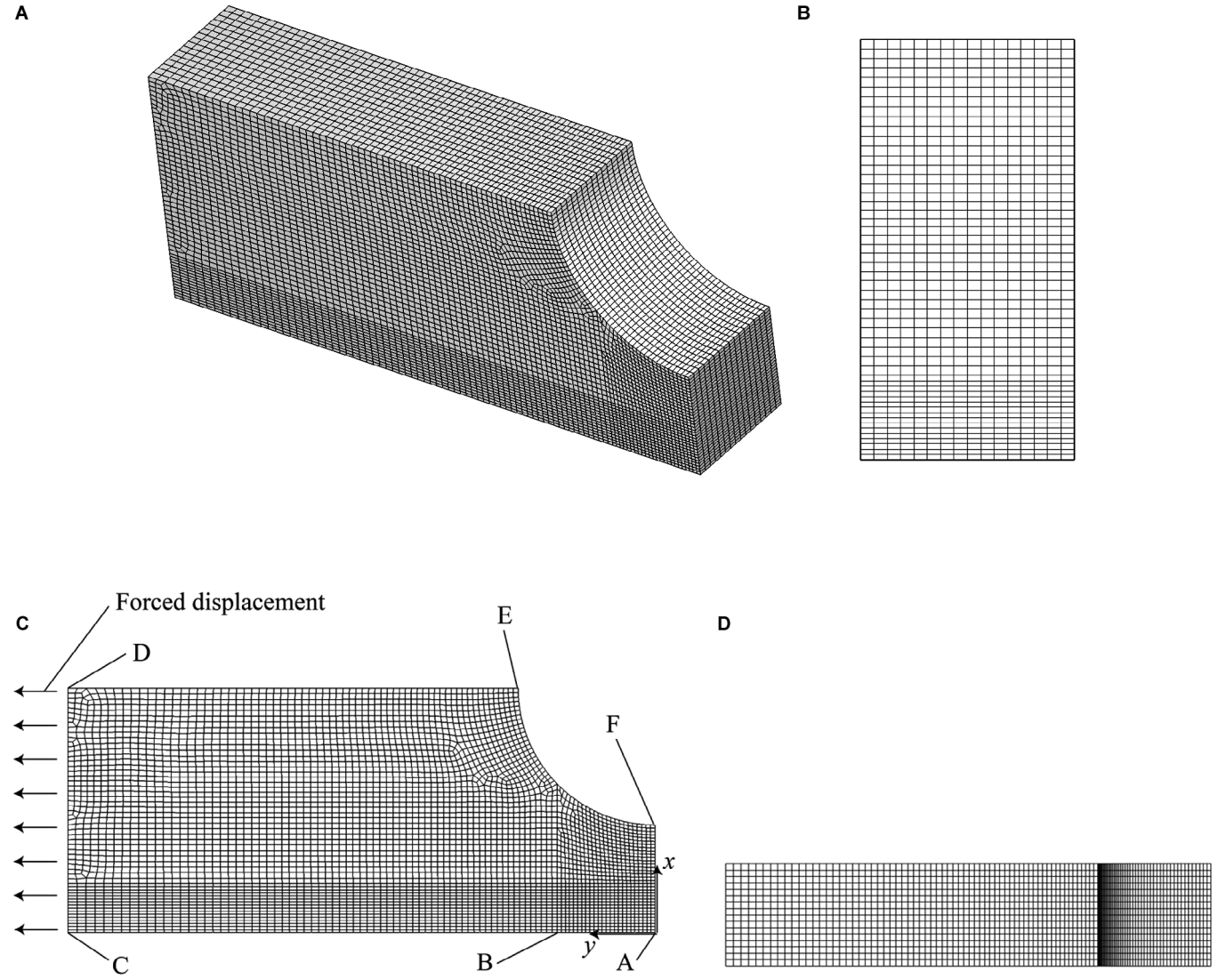

FIGURE 5. FE-mesh of notched rod model

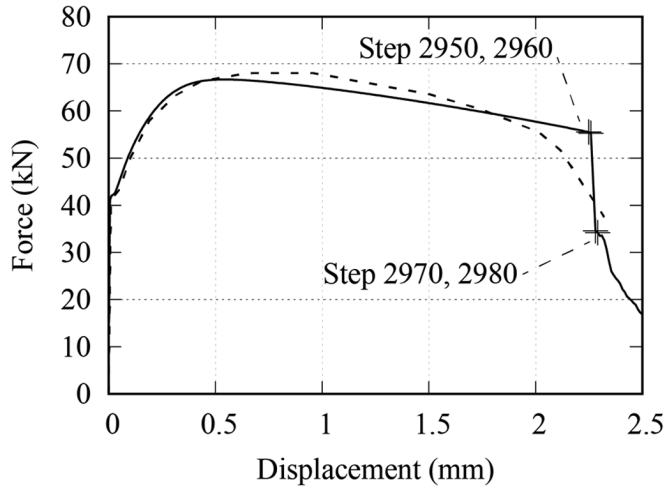

FIGURE 6. Load–displacement relation of notched rod; solid line: analysis, dotted line: experiment[34]

analysis result is plotted with solid line in Figure 6, where the axial reaction force is multiplied by 4 to obtain the load on the whole section of the rod. The maximum load obtained by analysis is 66.674 kN at $U = 0.544$ mm, which is close to the experimental result, and rapid decrease of load occurs at $U = 2.12$ mm. It is notable that the analysis can continue to trace the degrading load–displacement relation after the fracture.

The deformed shapes at the initial state (Step 0), the maximum load (Step 1 080), and the initiation of fracture (Step 2 950) are shown in Figure 7, where the black part is due to overlap of the mesh lines. The displacement and force at Step 2 950 is indicated in Figure 6 with + mark. The results show that the necking behavior can be successfully simulated by the linear hexahedral solid element with selective reduced integration for the volumetric strain. However, the purpose of this analysis is not to show that necking can be simulated, but to present a method for simulating the stiffness deterioration after fracture using an implicit time integration method.

Close view at the center is shown in Figure 8 for several steps after fracture, where the displacements and forces at

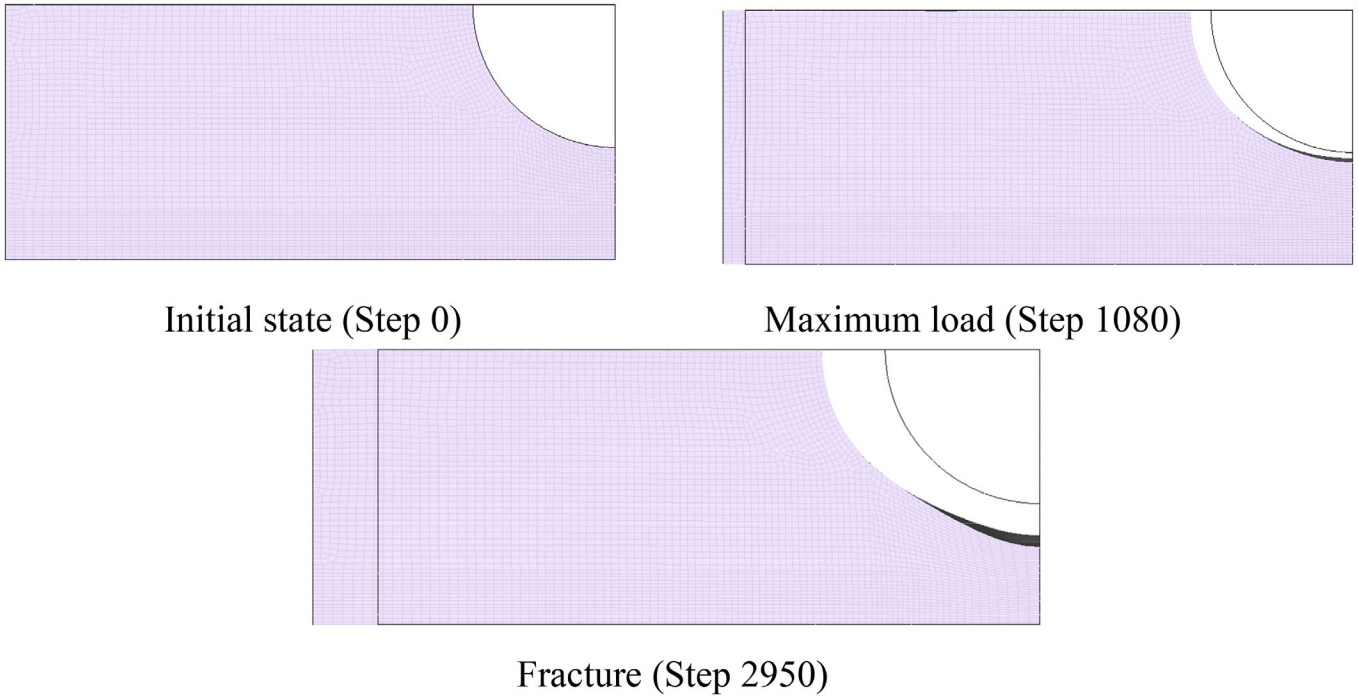

FIGURE 7. Deformed shapes at initial state, maximum load, and initiation of fracture

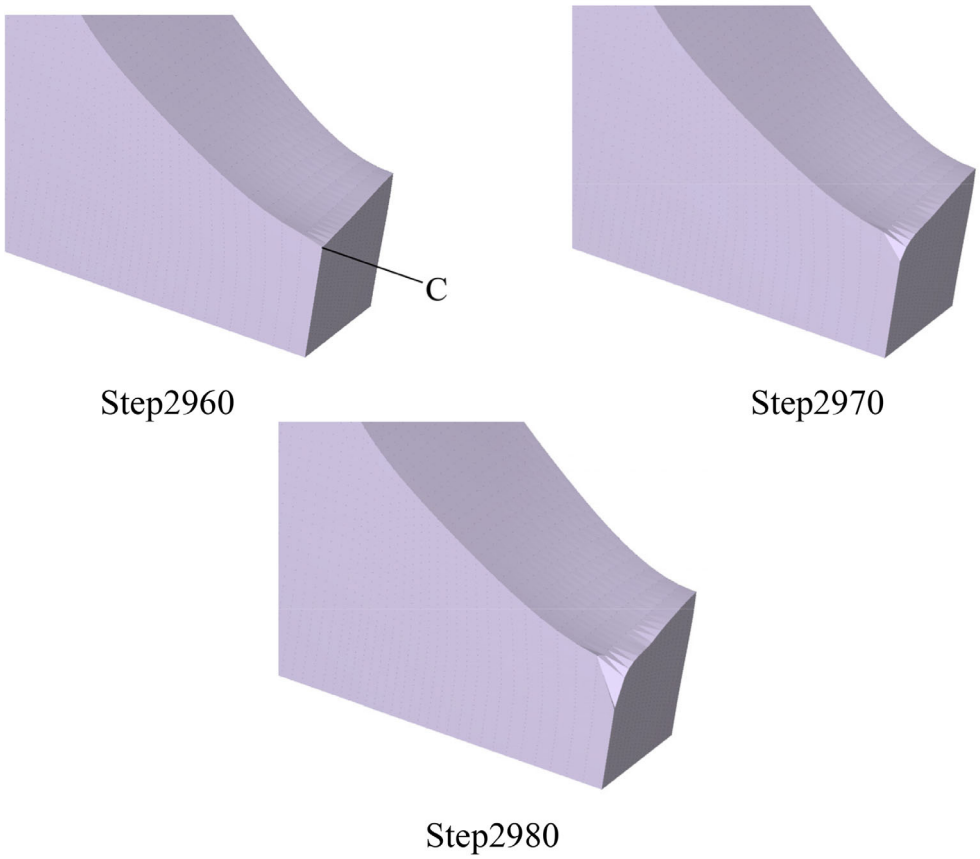

FIGURE 8. Close view of deformation after fracture

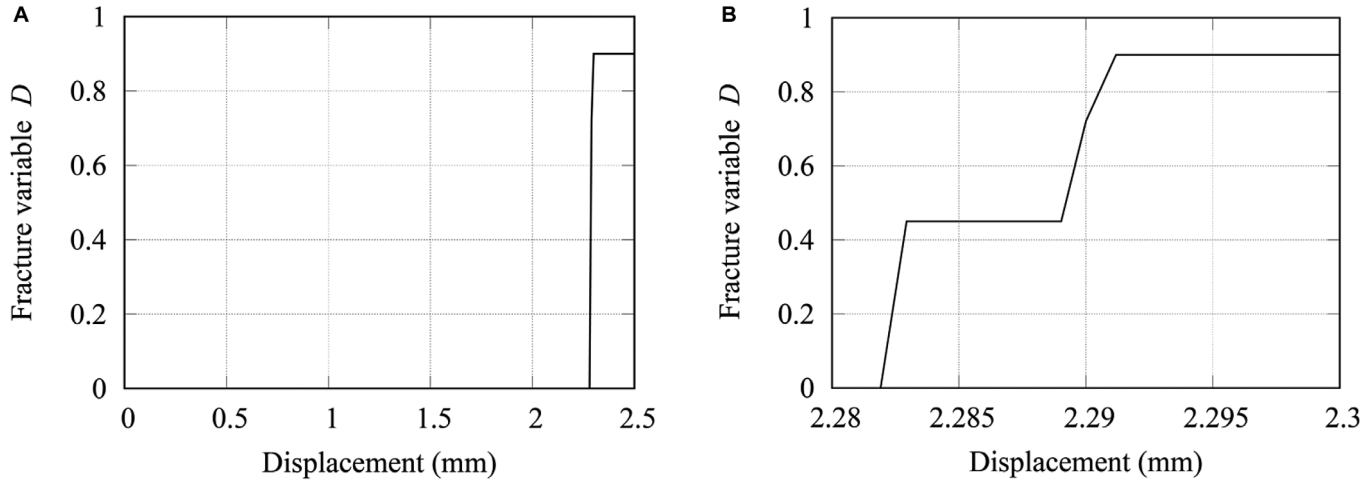

FIGURE 9. History of fracture variable of element C with respect to displacement; (A) whole loading history, (B) close view at initiation of fracture

these steps are indicated in Figure 6 with + marks, where Steps 2 950 and 2 960, and Steps 2 970 and 2 980, respectively, are almost duplicate in the figure. It is seen that large deformation propagates from the notch surface to the center of the rod. The stress strain relation in Figure 2B ensures increase of the true stress during the progress of deformation, and the reduction of the force before Step 2 960 is due to the reduction of cross-sectional area of the center section (right side of the 1/8 model) associated with the necking, and the rapid reduction of the force after Step 2 960 is due to the fracture. History of the fracture variable is plotted in Figure 9A for the element connected to node C indicated in Figure 8. Note that the average value among eight integration points is plotted in the Figure. A close view at the initiation of fracture is plotted in Figure 9B, which shows the stepwise increase of fracture variable D to the upper bound 0.9 at the initiation of fracture.

4. Double Notched Plate

To verify the proposed ductile fracture model and further demonstrate the ability of simulating stiffness degrading process due to ductile fracture, a forced displacement analysis is carried out for a double notched plate as shown in Figure 10, which was investigated in Refs. 35 and 36. The plate has circular notches at the two corners, and its thickness is 1.0 mm. The boundary conditions are specified in the figure, and forced y-directional displacement is applied along the upper edge. The nominal size of the mesh for automatic mesh generation is 0.1 mm. A bilinear elastoplastic material is assumed, and Young's modulus, Poisson's ratio, yield stress, and hardening coefficients are 180 GPa, 0.28022, 443.0 MPa, and 300 MPa, respectively.

Deformation under forced displacement is simulated for various (α_i, D_i) values listed in Table 1 to investigate the effect of these parameters on the response properties. Note that fracture is not considered in Case 1. The relations between y-directional displacement U and the total reaction force are obtained as shown in Figure 11. The deformed shapes at $U = 0.6$ and 1.0 are shown in Figures 12A and B, respectively, for Case 5, where the contour represents the equivalent plastic strain. Because no fracture occurs at $U = 0.6$, the shape in Figure 12A represents the deformation at $U = 0.6$ for all cases.

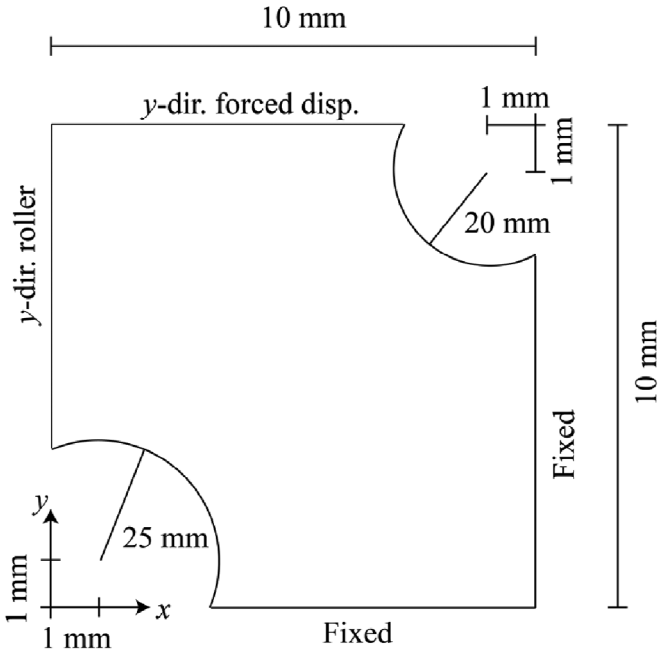

FIGURE 10. A double notched plate[35,36]

TABLE 1. Parameter sets for Cases 1–7 of double notched plate

	(α_1, D_1)	(α_2, D_2)	(α_3, D_3)
Case 1	(1.30, 0.0)	(1.50, 0.00)	(1.70, 0.00)
Case 2	(1.30, 0.0)	(1.50, 0.20)	(1.70, 0.95)
Case 3	(2.00, 0.0)	(2.20, 0.20)	(2.40, 0.95)
Case 4	(1.30, 0.0)	(3.30, 0.20)	(4.30, 0.95)
Case 5	(1.30, 0.0)	(2.80, 0.20)	(4.30, 0.99)
Case 6	(1.30, 0.0)	(2.80, 0.20)	(4.30, 0.60)
Case 7	(1.30, 0.0)	(2.80, 0.20)	(4.30, 0.80)

Therefore, a concentrated shear failure can be simulated without using the fracture variable. As seen from Figure 11A, no steep stiffness degradation occurs if ductile fracture is not

considered. Obviously, a larger α_1 value leads to a larger displacement at the initiation of fracture, which is also delayed by assigning a larger value for the difference between α_1 and α_2. It is also clearly observed that a larger value of D_3 leads to more rapid decrease of the reaction force. The reaction force reduces stepwise as strain localization occurs in multiple elements successively and stops because deformation is controlled by forced displacement.

5. Component Frame of Moment Frame

FE-analysis is carried out for a beam-column model as shown in Figure 13. An experiment under cyclic static deformation was carried out in Ref. [37]. The column has pin supports A and B, and a forced z-directional displacement (positive for upward displacement) is applied at the beam end C, where the out-of-plane displacement and rotations are constrained. All parts of the beam, column, and joint are divided into linear hexahedral elements with selective reduced integration. The sizes of the elements near the access hole are about 2.5 mm, and the total numbers of nodes and elements are 268 656 and 210 952, respectively.

The rotation angle of beam θ, excluding the rotation of the connection, is defined as

$$\theta = \left[U_z^{\mathrm{C}} - \left(U_z^{\mathrm{D}} + U_z^{\mathrm{E}}\right)/2\right]/(3000 - B/2) - \left(U_x^{\mathrm{D}} - U_x^{\mathrm{E}}\right)/H \quad (7)$$

where U_j^i is the j-directional displacement at point i, B is the width of column, and H is the height of beam. Let θ_{P} denote the value of θ when the bending moment at the beam-to-column connection reaches the fully plastic moment. The value of θ_{P} is 0.0082 according to Ref. [37]. A z-directional forced displacement is applied at the beam end so that the rotation angle of beam between the column face of the beam-to-column connection and the beam end obeys the pattern in Figure 14.

The sections of beam and column are H-450 × 200 × 9 × 14 (I-section) and SHS-350 × 12 (square hollow section), respectively, and the thickness of diaphragm is 19 mm. The materials are SS400 (JIS G 3101), STKR400 (JIS G 3466),

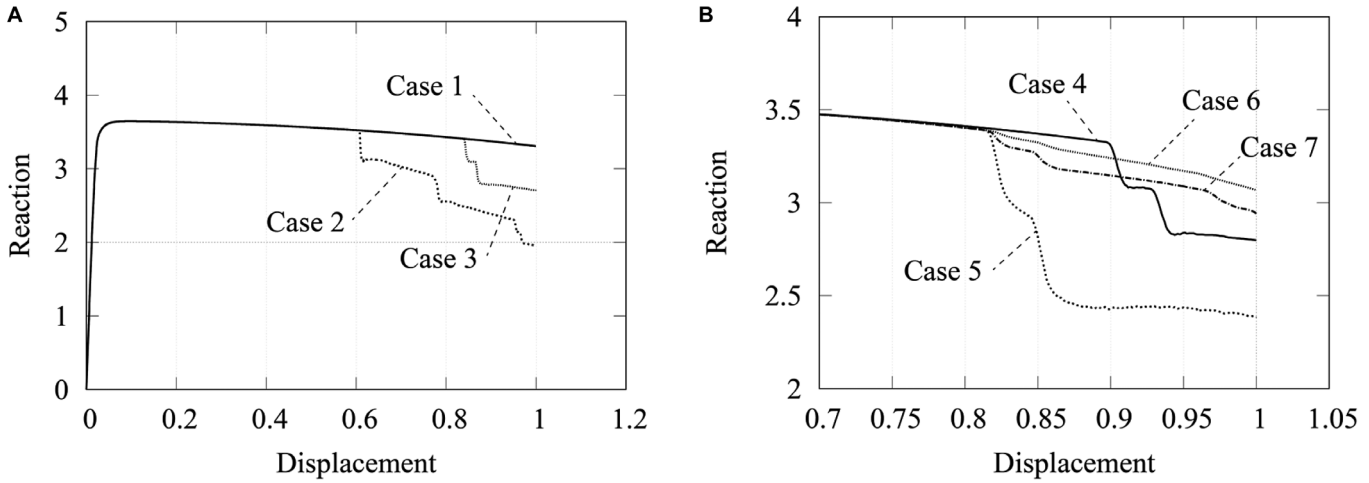

FIGURE 11. Relations between y-directional displacement (mm) and reaction force (kN); (A) Cases 1–3, (B) Cases 4–7 (close view near fracture)

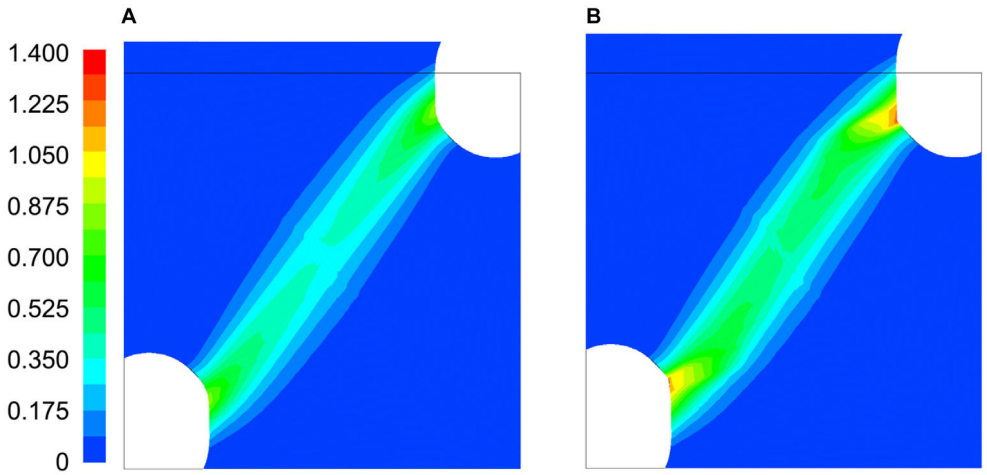

FIGURE 12. Deformed shape and equivalent plastic strain of Case 5; (A) $U = 0.6$, (B) $U = 1.0$

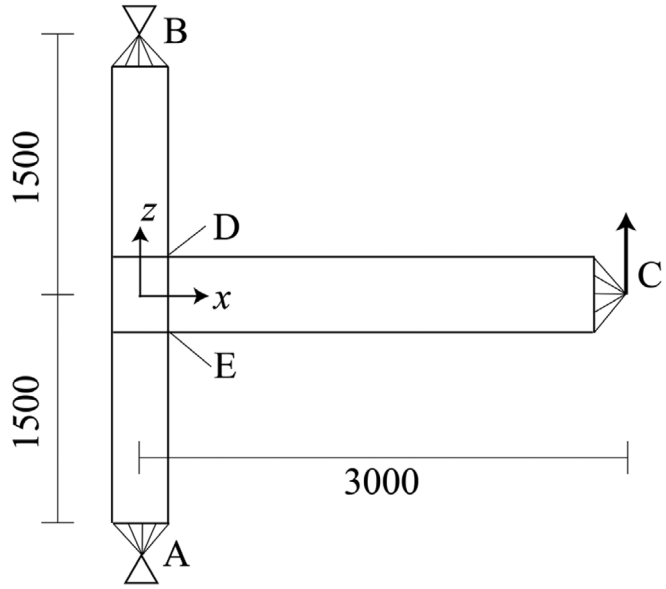

FIGURE 13. Beam-column model (unit: mm)

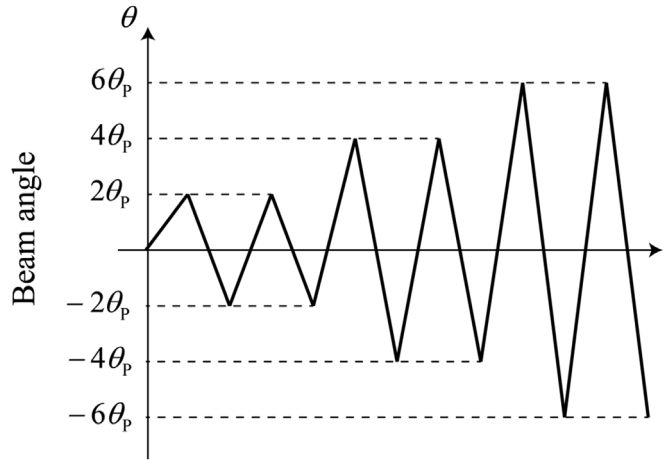

FIGURE 14. Cyclic loading pattern

TABLE 2. Measured thickness t, yield stress σ_Y, and tensile strength σ_U of parts[37]

	t (mm)	σ_Y (MPa)	σ_U (MPa)
Beam Flange	13.5	311	465
Beam Web	8.4	381	491
Diaphragm	18.6	319	462
Column	11.1	282	435

and SS400 by Japanese specification, respectively, for beam, column, and diaphragm. The measured thickness t, yield stress σ_Y, and tensile strength σ_U of the parts are listed in Table 2. The hardening coefficients are identified from the result of the material test for each part.[37] The relation between the uniaxial true stress and strain is plotted in Figure 15 for each component of the frame members. Note that the lower bound $E/100$ is given for the hardening coefficients, and the parameters for cyclic deformation are assigned based on the results in Ref. [20]. Although a detailed rule is proposed in Ref. [20] for incorporating the special characteristics for reloading to the yield plateau, it is simply ignored here because it is irrelevant to the fracture in a large strain range. Artificial damping coefficient is assigned especially in the plastic loading range to avoid divergence of the Newton–Raphson iteration. Although the displacement increment varies with the cycles, its value is approximately 0.27 mm in the elastic range, and 0.1 mm in the elastoplastic range.

Figure 16 shows the relation between the rotation angle of beam and the bending moment at the column face of the beam-to-column connection obtained by the experiment. In the experiment, a small crack of 0.45 mm was observed at the bottom of access hole in the first negative cycle of the amplitude $4|_P$, and the maximum load was reached at the first cycle of the amplitude $6\theta_P$. Finally, connection between the flange and the column ruptured at the first negative cycle of $6\theta_P$.

Analysis is first carried out by assigning forced displacement at node C computed from the target loading angle pattern in Figure 14, i.e., 0.0164, 0.0286, and 0.0428 rad for $2\theta_P$, $4\theta_P$, and $6\theta_P$, respectively, neglecting the rotation of the connection. Then, the rotation angle of beam is computed using Equation (7), and the difference between the target and computed values is added at each load reversal point to trace the target angle pattern more accurately.

We consider two cases of fracture parameter. In Case 1, the same fracture parameters as the notched rod are used. The relation between the average beam angle and the bending moment is plotted in Figure 17, which is close to the experimental result up to the cycles of $\pm 4\theta_P$. However, in this case, no ductile fracture is observed. Therefore, in Case 2, the deformation parameters, α_1, α_2, and α_3 in Figure 1 are reduced to $(\alpha_1, D_1) = (1.30, 0.0)$, $(\alpha_2, D_2) = (1.35, 0.2)$, $(\alpha_3, D_3) = (1.40, 0.9)$.

The moment-rotation relation for Case 2 is plotted in Figure 18, which is also close to the experimental result up to the cycles of $\pm 4\theta_P$. However, steep degradation of moment observed in the experiment at the second cycle of $-6\theta_P$ could not be numerically simulated. Deformation near the beam-to-column connection at each end of the half cycle is shown in Figure 19, where the contour represents the equivalent stress. Note that the same color range is used for contours in all figures. We can observe clear local buckling in the flanges from the first cycle of $4\theta_P$.

Deformed shape of the beam at the connection (column face) at each end of the half cycle for Case 2 is shown in Figure 20, where the contour represents the fracture variable D. The nodal value of D in the figure is extrapolated from the integration points; therefore, the value may slightly exceed the maximum value 0.9. However, the contour is truncated to the range between 0 and 0.9. Note that the upper flange, which is compressed by the forced deformation, is shown in Figure 20A, C, and E, while the lower flange is shown in Figure 20B, D, and F. Although no steep degradation of force is observed, fracture is confirmed to exist at the end of access hole and the corner of the flange connecting to the diaphragm of the joint. It is notable that very large tensile deformation exists in the web elements at the end of access hole.

In the experiment, a local buckling of about 30 mm was observed at the first cycle of $+6\theta_P$, whereas the value by analysis was 46 mm. As local buckling is very sensitive to the material parameters and support conditions, it is very difficult to have the same value between experiment and numerical

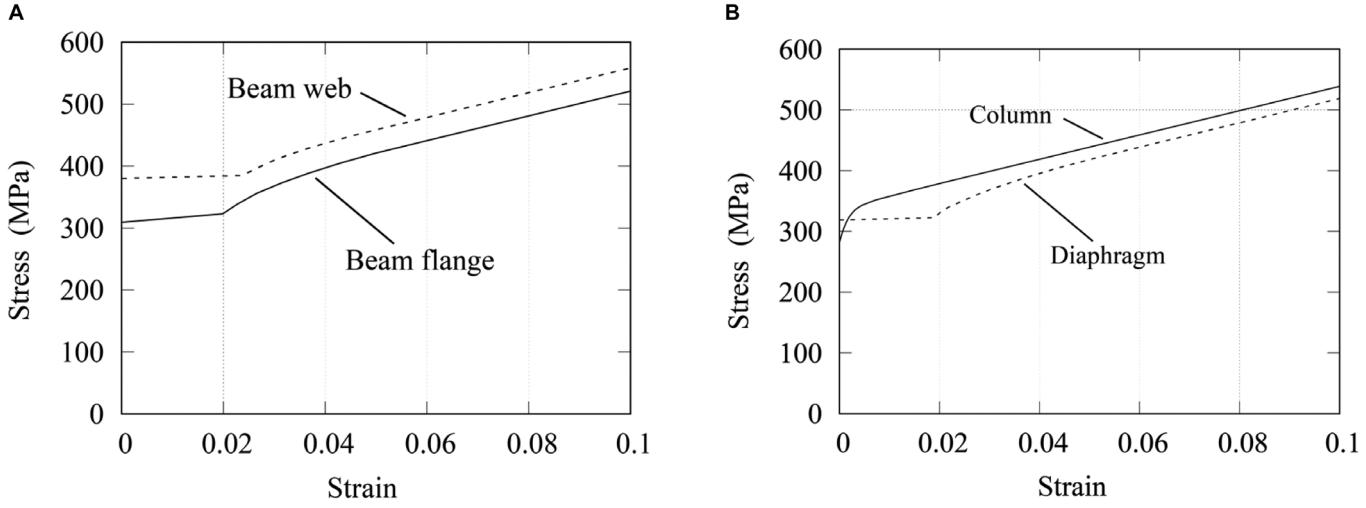

FIGURE 15. Relation between true stress and stress of parts; (A) beam web and flange, (B) column and diaphragm

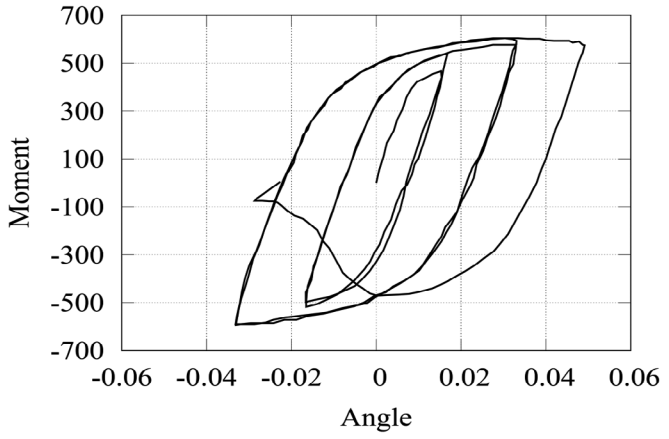

FIGURE 16. Relation between beam angle and bending moment (kNm): experimental result[37]

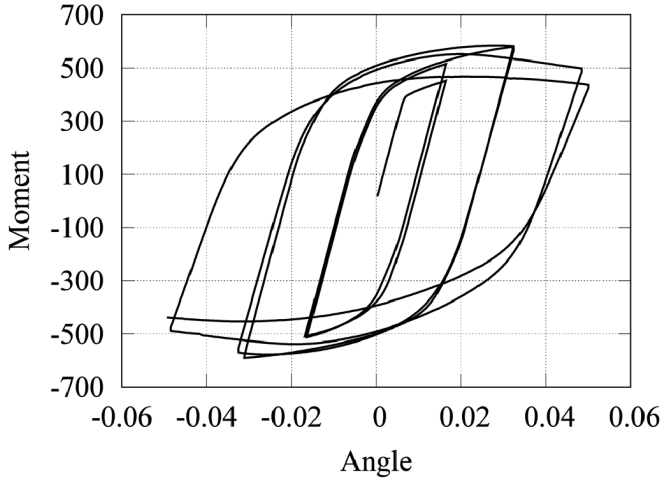

FIGURE 17. Relation between beam angle and bending moment (kNm): Case 1

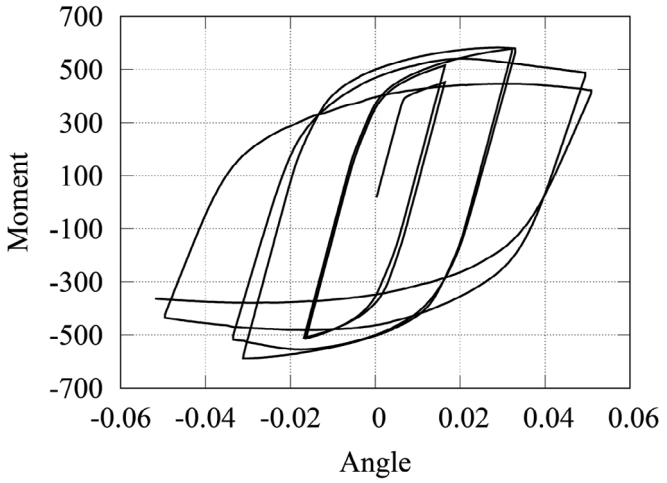

FIGURE 18. Relation between beam angle and bending moment (kNm): Case 2

analysis when the cyclic material property is unknown. Also, there are some uncertainties in the boundary conditions. Therefore, it is not reasonable to demand exact quantitative agreement between the single experimental result and simulation without considering uncertainty in the parameters. However, it is important that the deformation localization at the connection leading to stiffness deterioration can be simulated, as shown in Figures 18 and 20, using the proposed method.

To investigate the effect of (α_i, D_i) values on the responses of the component frame model, for additional analyses are carried out with different parameter sets as shown in Table 3, where Case 2 is also listed for comparison. Note that the values of α_2 and α_3 are greater than α_1 by 0.05 and 0.10, respectively, for all cases. The results after second $-4\theta_P$ are plotted in Figures 21A–C. It is observed from Table 3 and Figure 21A that a larger value of α_1 leads to a larger maximum bending moment, although the difference between Cases 2 and 4 with $\alpha_1 = 1.30$ and 1.10, respectively, is not very large. It is also seen from Figure 21B and C that difference between the cases

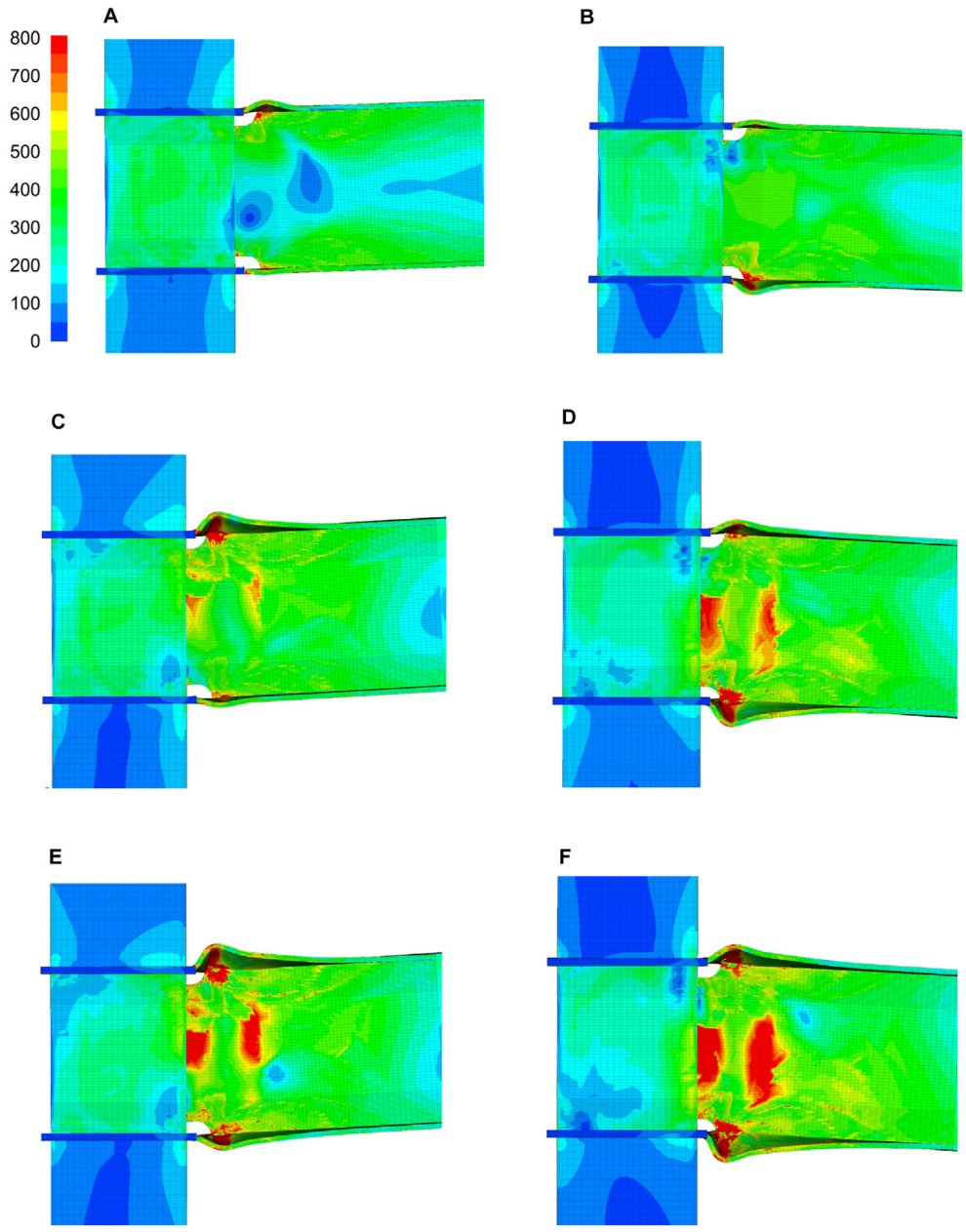

FIGURE 19. Deformed shape and equivalent stress (MPa) at beam-to-column connection; (A) $4\theta_P$:2nd, (B) $-4\theta_P$:2nd, (C) $6\theta_P$:1st, (D) $-6\theta_P$:1st, (E) $6\theta_P$:2nd, (F) $-6\theta_P$:2nd

with $D_3 = 0.90$ and 0.95 is not significant. However, the analysis stopped before reaching the final loop if $D_3 = 0.95$.

6. Conclusions

A ductile fracture model has been combined to the cyclic elastoplastic constitutive model of steel material for application of large-scale implicit finite element analysis. The SMCS rule considering the stress triaxiality is used for detecting initiation of fracture, and the degradation after fracture is modeled using a piecewise linear relation between the fracture variable and the deformation variable, which is a function of the equivalent plastic strain. The fracture model is implemented to the E-Simulator based on ADVENTURECluster as a user function.

Important advantage of the proposed procedure is that positive definiteness of the material tangent stiffness matrix is always maintained. Unstable response after deterioration (degradation) of stiffness and strength due to ductile fracture is simulated by scaling the stress, yield stress, backstress, Young's modulus, and hardening coefficient based on the fracture variable, and carrying over the unbalanced load to the next step, while maintaining stability during Newton–Raphson iteration. Although the equilibrium state after convergence is a tentative state, the unbalance force is negligibly small and can be reduced in the next step if a small increment is adopted.

Uniaxial tension analysis is carried out for a notched rod to verify the accuracy and ability of simulating degrading strength after fracture. It is notable that degradation of the load

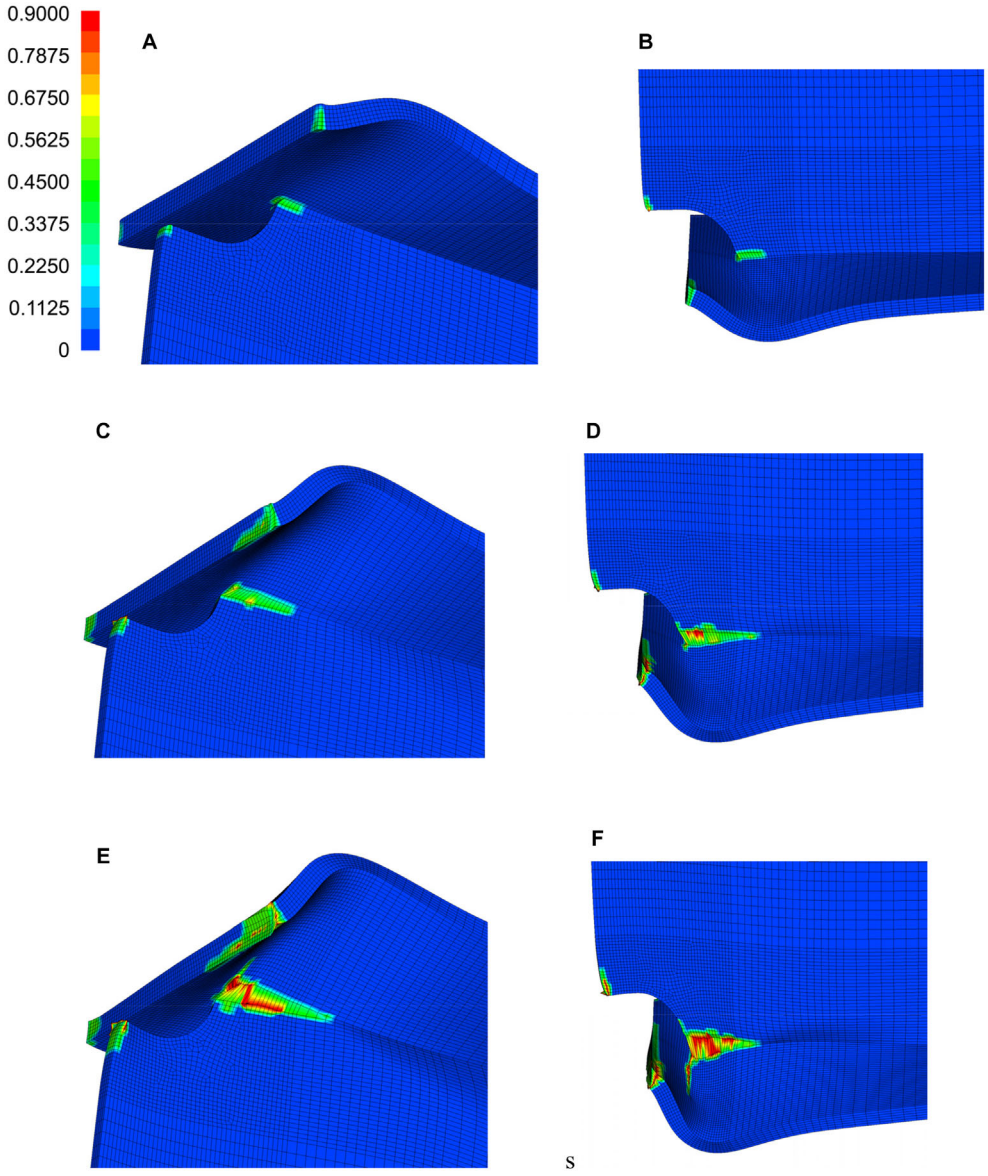

FIGURE 20. Deformed shape and fracture variable at beam-to-column connection; (A) $4\theta_P$:2nd, (B) $-4\theta_P$:2nd, (C) $6\theta_P$:1st, (D) $-6\theta_P$:1st, (E) $6\theta_P$:2nd, (F) $-6\theta_P$:2nd

TABLE 3. Parameter sets for Cases 2–6 of component frame

	(α_1, D_1)	(α_2, D_2)	(α_3, D_3)
Case 2	(1.30, 0.0)	(1.31, 0.20)	(1.32, 0.90)
Case 3	(1.50, 0.0)	(1.51, 0.20)	(1.52, 0.90)
Case 4	(1.10, 0.0)	(1.11, 0.20)	(1.12, 0.90)
Case 5	(1.30, 0.0)	(1.31, 0.20)	(1.32, 0.95)
Case 6	(1.50, 0.0)	(1.51, 0.20)	(1.52, 0.95)

due to necking corresponding to the reduction of cross-sectional area can be simulated using the proposed model and the linear hexahedral solid element with reduced integration of the volumetric strain.

A method has been proposed for simulating stiffness degradation due to strain localization after ductile fracture. The strain localization after necking have been successfully simulated for the monotonic tensile test of a notched bar. Applicability of the model to a large-scale FE-analysis is demonstrated by cyclic analysis of a beam-column model in comparison to the experimental results. It has been shown that the relation between the bending moment at the column face of the connection and the rotation angle of beam can be accurately simulated using the proposed model. Although the drastic degradation by ductile fracture could not be simulated, the fracture near the access hole of the connection clearly appears as a very large tensile deformation in the web elements. Very small increments have been adopted for these numerical examples to ensure accuracy of the responses. The effect of magnitude of increment on accuracy of the results may be a subject of future research.

For application of the proposed method to evaluate the ductile fracture behavior of structure or structural component, the appropriate values of parameters such as α_i and D_i should be

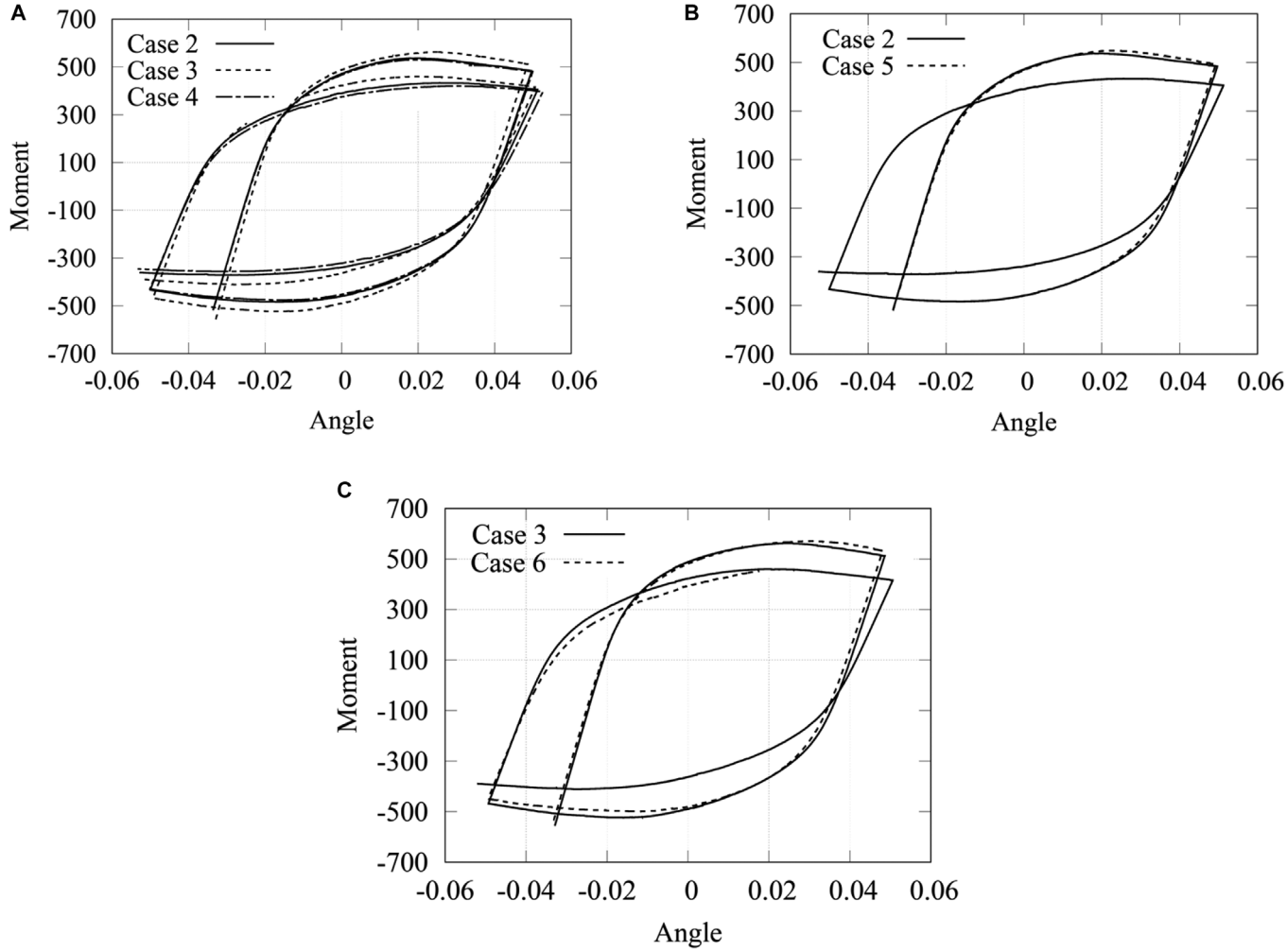

FIGURE 21. Comparison of relations between beam angle and bending moment (kNm); (A) Cases 2, 3, and 4, (B) Cases 2 and 5, (C) Cases 3 and 6

determined from a material test or a small scale structural test. α_1 is determined by initiation of fracture, difference between α_1 and α_2 as well as the value of D_2 is determined by how rapidly fracture progresses, and α_3 and D_3 are determined by the loss of load-bearing capacity. These values depend on the size of FE-mesh and the distance from the stress-concentration part as discussed in Refs. [13–16].

Acknowledgments

This study is a part of E-Defense Seismic Experimental Study and E-Simulator Development Project at the National Research Institute for Earth Science and Disaster Resilience (NIED). The authors acknowledge the valuable comments from Dr. Takuzo Yamashita at NIED as well as contribution from the committee members and the financial support of NIED. This work is also supported by JSPS KAKENHI Grant Number JP19H02286.

Disclosure

The authors have no conflict of interest.

Data availability statement

The data that support the findings of this study are available from the corresponding author upon reasonable request.

References

1 Matsui R, Urui S, Tokuno M, Takeuchi T. Seismic performance assessment for steel frames considering fracture of beams and braces. *J Struct Constr Eng*, 2014;**80**(717):1745–1754. (in Japanese)
2 Kim T, Kim J. Collapse analysis of steel moment frames with various seismic connections. *J Constr Steel Res* 2009;**65**:1316–1322.
3 Okazaki T, Lignos DG, Hikino T, Kajiwara K. Dynamic response of a chevron concentrically braced frame. *J Struc Eng* 2013;**139**(4): 515–525.
4 Isobe D, Toi Y. Analysis of structurally discontinuous reinforced concrete building using the ASI technique. *Comp Struct* 2000;**76**(4);471–481.
5 Xiang P, Qing Z, Jia LJ, Wu M, Xie J. Damage evaluation and ultra-low-cycle fatigue analysis of high-rise steel frame with mesoscopic fracture models. *Soil Dynamics and Earthquake Eng*. 2020; **139**: Paper No. 106283.
6 Huang X, Tong L, Zhou F, Chen Y. Prediction of fracture behavior of beam-to-column welded joints using micromechanics damage model. *J Constr Steel Res* 2009;85:60–72.
7 Mizushima Y, Mukai Y, Namba H, Taga K, Saruwatari T. Super-detailed FEM simulations for full scale steel structure caused fatal rupture at its joint parts between members. *J Struct Constr Eng* 2016;**81**(719):61–70. (in Japanese)
8 Wang Y, Arakida R, Chan I, Koetaka Y, Nakano T. Cyclic behavior of panel zone in beam-column subassemblies subjected to bidirectional loading. *J Constr Steel Res* 2018;**143**:32–45.
9 Sawamoto Y, Ohsaki M. Evaluation on plastic deformation capacity of steel beam ends with local buckling and fracture under cyclic loading using FE analysis. *J Struct Constr Eng* 2020;**85**(767):105–115. (in Japanese)
10 Huang Y, Mahin S. Evaluation of steel structure deterioration with cyclic damaged plasticity. *Proc. 14th World Conference on Earthquake Engineering (14WCEE)*, Beijing. 2008; Paper No. 14–0240.

11 Rice JR, Tracey DM. On the ductile enlargement of voids in triaxial stress fields. *J Mech Phys Solids* 1969;**17**(3):201–217.
12 Hancock JW, Brown DK. On the role of strain and stress state in ductile failure. *J Mech Phys Solids* 1983;**31**(1):1–24.
13 Chi WM, Kanvinde AM, Deierline GG. Prediction of ductile fracture in steel connection using SMCS criterion. *J Struct Eng* 2006;**132**(2):171–181.
14 Hancock JW, Mackenzie AC. On the mechanism of ductile failure in high-strength steels subjected to multi-axial stress-states. *J Mech Phys Solids* 1976;**24**:147–169.
15 Kanvinde AM, Deierline GG. *Micromechanical Simulation of Earthquake Induced Fracture in Steel Structures*. Technical Report TR145. Stanford, CA: Blume Center, Stanford Univ; 2004.
16 Kanvinde AM, Deierline GG. Void growth model and stress modified critical strain model to predict ductile fracture in structural steels. *J Struct Eng* 2006;**132**(12):1907–1918.
17 Ohsaki M, Nakajima T. Optimization of link member of eccentrically braced frames for maximum energy dissipation. *J Constr Steel Res* 2012;**75**:38–44.
18 Kanvinde AM, Marshall KS, Grilli DA, Bomba G. Forensic analysis of link fractures in eccentrically braced frames during the February 2011 Christchurch earthquake: testing and simulation. *J Struc Eng* 2014;**141**(5):04014146.
19 ADVENTURECluster, https://www.scsk.jp/sp/advc/index.html
20 Ohsaki M, Miyamuta M, Zhang JY. A piecewise linear isotropic-kinematic hardening model with semi-implicit rules for cyclic loading and its parameter identification. *Comput Model Eng Sci* 2016;**111**(4):303–333.
21 Miyamura T, Yamashita T, Akiba H, Ohsaki M. Dynamic FE simulation of four-story steel frame modeled by solid elements and its validation using results of full-scale shake-table test. *Earthquake Eng Struct Dyn* 2015;**44**:1449–1469.
22 Tagawa H, Miyamura T, Yamashita T, Kohiyama M, Ohsaki M. Detailed finite element analysis of full-scale four-story steel frame structure subjected to consecutive ground motions. *Int J High-Rise Buildings* 2015;**4**(1):65–73.
23 Pal MK, Yamashita T, Miyamura T, Ohsaki M. A comprehensive numerical simulation of steel-concrete composite beam incorporating compressive failure of concrete. *Int J Comput Methods* 2019;**16**(6):Paper No. 1840028.
24 Yamashita T, Ohsaki M, Kohiyama M, Miyamura Y, Zhang JY, Tagawa H. Detailed finite element analysis of composite beam under cyclic loads. *J Struct Constr Eng* 2014;**79**(704):1481–1490. (in Japanese)
25 Kim HS, Kim HS, Ryu WS. Finite element analysis of the onset of necking and the post-necking behaviour during uniaxial tensile testing. *Mater Trans* 2005;**46**(10) 2159–2163.
26 Okazawa S, Usami T, Noguchi H, Fujii F. Three-dimensional necking bifurcation in tensile steel specimens. *J Eng Mech* 2002;**128**(4): 479–486.
27 Dufalilly J, Lemaitre J. Modeling very low cycle fatigue, *Int J Damage Mech* 1995;**4**:153–170.
28 Lemaitre J. *A Course on Damage Mechanics*. Berlin: Springer-Verlag; 1992.
29 Lee J, Fenves GL. Plastic-damage model for cyclic loading of concrete structures. *J Eng Mech* 1998;**124**:892–900.
30 Fincato R, Tsutsumi S. Numerical modeling of the evolution of ductile damage under proportional and non-proportional loading. *Int J Solids Struct* 2019;**160**:247–264.
31 Chaboche JL. A review of some plasticity and viscoplasticity constitutive theories. *Int J Plasticity* 2008;**24**:1642–1693.
32 Gurson AL. Continuum theory of ductile rupture by void nucleation and growth: part I, yield criteria and flow rules for porous ductile media. *J Eng Mater Techol* 1977;**99**:2–15.
33 Kojic M, Vlastelica I, Zivkovic M. Implicit stress integration procedure for small and large strains of the Gurson material model. *Int J Numer Meth Eng* 2002;**53**:2701–2720.
34 Obata M, Mizutani A, Goto Y. The verification of plastic constitutive relation and its application to FEM analysis of plastic fracture of steel members. *J Japan Soc Civ Eng* 1999;**I-48**(626):185–195. (in Japanese)
35 Ambati M, Gerasimov T, De Lorenzis L. Phase-field modeling of ductile fracture. *Comput Mech* 2015;**55**: 1017–1040.
36 Mediavilla J, Peerlings RHJ, Geers MGD. Discrete crack modelling of ductile fracture driven by non-local softening plasticity. *Int J Numer Meth Engng* 2006;**66**:661–688.
37 Fukuoka D, Namba H, Morikawa S. E-defense shaking table test for full scale steel building on cumulative damage by sequential strong ground motion: part 2, Subassemblage tests. *Proc Annual Meeting of AIJ*. 2014; Structures III:977–978, Paper No. 22489. (in Japanese)

How to cite this article: Ohsaki M, Fujiwara J, Miyamura T, Namba H. Implicit finite element analysis of ductile fracture of a steel frame under cyclic deformation. *Jpn Archit Rev*. 2022;5:150–163. https://doi.org/10.1002/2475-8876.12264